Geothermics 111 (2023) 102705

Contents lists available at ScienceDirect

Geothermics

journal homepage: www.elsevier.com/locate/geothermics

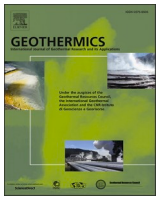

In-situ flow visualization with Geo-Positron-Emission-Tomography in a granite fracture from Soultz-sous-Forêts, France

Janis Leon Pingel [a], Johannes Kulenkampff [b], Daniel Jara-Heredia [a], Madeleine Stoll [a], Wenyu Zhou [b], Cornelius Fischer [b], Thorsten Schäfer [a,*]

[a] Institute for Geosciences, Friedrich-Schiller-University Jena, 07749 Jena, Germany
[b] Reactive Transport Department, Institute of Resource Ecology, Helmholtz-Zentrum Dresden-Rossendorf, 04318 Leipzig, Germany

ARTICLE INFO

Keywords:
Positron emission tomography
Single fracture
Fluid flow
Flow channeling
Fracture aperture
COMSOL

ABSTRACT

We investigate the fluid flow field in a fractured granite core sample. Sequential imaging with Positron-Emission-Tomography (PET) allows direct reconstruction of flow streamlines, thus providing a unique insight into the fluid dynamics of complex fractured crystalline materials. Pulse migration experiments using the positron-emitting radionuclide $^{18}F^-$ as tracer were conducted on a fractured granitic drill core, originating from a depth of 1958 m of the Enhanced Geothermal System (EGS) reference site at Soultz-sous-Forêts, France. The flow field was analyzed as a function of in- and outlet positions across the fracture, as well as applied flow rates. Different flow path characteristics were identified. Both the fracture aperture variation and the topography of the fracture surface affect the flow field with consequences on flow channeling and preferential flow paths. Furthermore, pulse migration experiments were also numerically simulated with a 2.5D model using COMSOL Multiphysics®.

While the higher flow rate experiments show wider and higher dispersion of the flow path, lower velocity results in more localized flow and channeling behavior. This type of study thus yields enhanced experimental insights into the hydrodynamics of fracture flow and its relation to the rough structure of a single fracture, compared to input-output experiments. It can help to validate model simulations and experimentally determine hydrodynamic parameters needed for reactive transport modeling that are otherwise estimated with a high degree of uncertainty.

1. Introduction

Geologic materials tend to be heterogeneous with respect to porosity, permeability, and their mineralogical composition. Hence, it is a challenging task to study transport processes at the pore scale in laboratories or in the field. The material is usually considered a "black-box" as typical input-output experiments miss heterogeneous effects like preferential transport (Kulenkampff et al., 2016). Thus, detailed structural analyses are necessary to tackle fluid hydraulics in fractured rocks, due to their natural anisotropy. Thereby, transport paths depend on the surface topography (i.e. aperture, curvature, surface roughness). Information on the evolution of flow patterns and a possible flow channeling behavior at the flow-wetted fracture surfaces are later used for retention properties (i.e. local residence time, local flow pattern, local hydro-geochemistry).

For the direct investigation of flow path evolution, a variety of tools are available. Besides methods like Positron-Emission-Tomography, other techniques like Magnetic Resonance Tomography have in the past been used to quantify the heterogeneity of flow fields as demonstrated by e.g. (Baumann et al., 2000). In combination with imaging techniques like micro Computer Tomography (μ-CT), Scanning Electron Microscopy, or Transmission Electron Microscopy, it is possible to characterize three-dimensional structures with a high level of detail. For investigating in-situ flow paths and mass transport behavior, we use the PET-method, which has yet been rarely applied for geoscientific applications. The PET-method is based on the works of Ter-Pogossian and Phelps in the 1970s (Ter-Pogossian et al., 1975) and was introduced as a nuclear imaging technique for medical, clinical, and pharmaceutical issues. Subsequently, it was widely used as an early detection and staging method for many diseases such as cancer (Alauddin, 2011). To study the issues of flow and transport behavior within sealed materials such as enclosed drill cores, the PET-method was first adapted for geoscientific purposes in the late 1980s and is here referred to as GeoPET (van den Bergen et al., 1989; Benton and Parker, 1996). It has been continuously developed by different research groups i.e. (Kulenkampff

* Corresponding author.
E-mail address: thorsten.schaefer@uni-jena.de (T. Schäfer).

https://doi.org/10.1016/j.geothermics.2023.102705
Received 24 January 2023; Received in revised form 7 March 2023; Accepted 16 March 2023
Available online 21 March 2023

et al., 2013; Kulenkampff et al., 2008), who applied the method for quantitative spatiotemporal process monitoring in dense material, as well as (Fernø et al., 2015), who quantified fluid flow in sedimentary rocks by combining PET and computed tomography. Proving to be a valuable tool for quantitative in-situ investigations of fluid transport in porous and/or fractured geological materials, (Zahasky et al., 2019) further applied the method with respect to water resource and subsurface energy resource engineering research. μ-CT thereby allows a non-destructive detailed reconstruction of a rock sample and thus a structural characterization of its interior. Segmented μ-CT images, therefore, provide realistic boundary conditions for analyzing and interpreting PET images (Stoll et al., 2019; Huber et al., 2012). As they show the structural geometry in a high level of detail, they are also suited for setting up models for simulations on the pore scale. However, as structural models are ultimately limited by their resolution, they might miss significant features of the transport process below their detection limit. Specifically, details such as sub-resolution micro--fractures, sub-micron-sized pore-filling minerals as well as fracture surface asperities are usually not available in μ-CT datasets. Even though PET lags the level of visual detail provide by e.g. μ-CT, it shows transport with a higher degree of detail, limited only by a minimum detection amount of emitted positrons per frame (Kulenkampff et al., 2016).

The Soultz-sous-Forêts fracture sample stems from a medium where operating conditions (i.e. high flow rates) could establish turbulent flows (Kohl et al., 1997; Schill et al., 2017). Therefore inertial forces cannot be neglected and classical laminar flow fracture mathematical approaches should be reconsidered (Kolditz, 2001). Nevertheless, granitic fracture systems are also of interest for low-flow rate geo-engineering applications (Geckeis et al., 2004). Different mathematical formulations and conceptual models might be postulated for single fracture and fracture networks, but in general, they are based on the Navier-Stokes equations or simplifications such as the local cubic law (Brush and Thomson, 2003; Huang et al., 2021). Due to its complexity, the equations are usually resolved by numerical methods rather than analytical solutions such as finite elements (Huyakorn et al., 1983), lattice Boltzmann (Eker and Akin, 2006), or smoothed particle hydrodynamics (Tartakovsky and Meakin, 2005).

Understanding the issues of deep geothermal resources, which are often related to reactive transport processes, requires intimate knowledge of the fluid migration field in complex porous and fractured material, which is an outcome of inter alia GeoPET measurements. One of the main challenges of EGS is a detailed understanding of the physical and chemical processes at the heat-exchanging surface (i.e. the fracture surface). This area must be large enough to enable a sufficient heat transfer, but should not exceed a certain size in order to avoid hydrothermal alteration processes (Li et al., 2016). Similar requirements have to be matched in many applications of reservoir engineering; a possibly harmful alteration is frequently to be avoided or controlled for the contact area between the flowing water and the flow-wetted surfaces. Issues related to reactive transport, material-related influences, sustainability and upscaling, the larger geological background information, and the conjunction of all, can be solved with reactive transport laboratory studies in combination with model simulations of such systems.

We examined a naturally fractured granite core that has previously been investigated for input-output and modeling studies (Stoll et al., 2019). Beyond their model simulations focusing on the effects of fracture geometry on tracer breakthrough long-term tailing behavior, our experiments provide detailed experimental information on the first arrival times of the tracer (fastest flow paths) and the real internal fluid migration within the fracture for different hydrodynamic dipole conditions. Furthermore, we adapt a previous numerical model (Stoll et al., 2019), considering the decay and new boundary conditions in order to compare quantitative and qualitative experimental and numerical results.

2. Materials, methods, and numerical formulation

2.1. μ-CT and GeoPET

An overview μ-CT image of the complete core, including in- and outlets, and a fiducial marker for PET-CT co-registration was acquired with a Nikon XT H 225 scanner. The source parameters were 190 kV, and 175 μA, with a 2.5 mm Cu-filter for homogenization of the energy spectrum. The tomogram was reconstructed with the Nikon-OEM procedure, including beam-hardening correction, resulting in an image size of 1968×2079×2160 pixels with a voxel size of 72.6 μm.

For the GeoPET experiments, a ClearPET™-scanner (Elysia-Raytest) was used. It is a high-resolution scanner with a rotating gantry, designed for pre-clinical biomedical purposes. Inspired by the "ClearPET Neuro" at the Research Center Jülich (Ziemons et al., 2004), the scanner was tilted into a horizontal orientation (90°), enabling a vertical orientation of the drill core for fluid flow from bottom to top. This was set up to prevent gravitational influences and water breaks. Instead of an extensive device for horizontal gantry rotation, a lightweight rotation table was installed, turning the sample around its z-axis. The scanner features a standard voxel size of 1.15 mm, a cylindrical field of view with a diameter of 160 mm, and a length of 110 mm. Its gantry consists of 20 cassettes in a circular layout, with each having 10,240 scintillation crystals. A photomultiplier-crystal-combination of LuYAP ($Lu_{0.7}Y_{0.3}AlO_3$:Ce) and LYSO ($(Lu_{0.9}Y_{0.1})_2SiO_5$:Ce) crystals in a double layer structure with a size of 2 × 2 × 10 mm^3 serves for detection enhancement by directional filtering of the incoming photons. Initially, all detected events in the energy range from 250-750 keV are stored as single event files for later sorting into coincidence list-mode-files (LMF). The PET scanner thereby detects coincidences of pairs of annihilation photons, which occur when a slowed-down positron interacts with an electron (Kulenkampff et al., 2016). Its fundamental resolution limit is a function of the free path length of positrons in the matter, which is determined by the initial kinetic energy of the positron and the density (resp. scatter cross-section) of the medium (Levin and Hoffman, 1999). In water, this length is in the order of 1 mm but decreases with an increase in electron density (Berger et al., 2010). In a granite sample with more than 2.5 times higher density, this resolution limit is considerably smaller, as a Compton attenuation of 30 to 80% must be assumed (Kulenkampff et al., 2016). Thus, the image resolution is mainly determined by the properties of the detectors. PET yields a 3D data set of the tracer activity (concentration) with a high sensitivity and dynamic range. Reconstruction of one point of the tomogram requires the order of 10 events out of 10^7 that are typically recorded per frame (Kulenkampff et al., 2016). Based on the activity and half-life of the radio-tracer applied, the sensitivity of PET measurements can be as high as a picomole (10^{-12}) per microliter. Sequential imaging produces a spatiotemporal quantitative image of the concentration distribution, which is the most significant variable of reactive transport. Such sequences are utilized to calculate the flow vectors. Kulenkampff et al. (Kulenkampff et al., 2016) describe the statistical error in the order of ± 10%, based on the number of counts per voxel for the experiments and the radiotracer concentration used in this study.

As radiotracer, $^{18}F^-$was used for its favorable positron-emitting properties and a convenient half-life of 109.77 min (Kulenkampff et al., 2016). As Fluorine is an electronegative element, interaction such as electrostatic sorption with the generally negatively charged internal surface of the fracture is unlikely during the experiments. However, electro-repulsion effects between the surface and $^{18}F^-$ could occur.

2.2. Sample and fracture geometry

The porphyritic granite drill core was recovered from a depth of 1958 m of exploration well EPS-1 of the geothermal reference site in Soultz-sous-Forêts, France (Stoll et al., 2019). It is further described as minorly altered but having a single axial fracture separating the sample

in two halves. Furthermore, the sample length is 92.9 ± 0.3 mm with a diameter of 78.0 ± 0.4 mm.

After cutting and removing all loose parts with compressed air, the drill core was cast with epoxy resin into an acrylic glass casing (Fig. 1). A wedge-shaped widening of the fracture along the core boundary was sealed with two-component epoxy adhesive, in order to close this artificial major flow path. To minimize the artificial dispersion inside the cell, two endcaps each having three discrete outlets, situated alongside the fracture, were attached, with rectangular rubber lips as sealing on both ends. (Stoll et al., 2019)

The fracture geometry was analyzed using μ-CT imaging. The segmented model shows a nearly continuous aperture with an average value of 0.619 mm and a resolution of 72.6 μm (Fig. 2). The average aperture value differences between (Stoll et al., 2019) μ-CT results (0.357 mm) and our results probably steam from three sources: (i) different μ-CT machines and thus the resolutions obtained (72.6 > 60 μm), (ii) differences in the applied post-processing algorithms and (iii) different segmentation (threshold) judgments applied by the users. Contact areas (aperture = 0, or below μ-CT resolution) are uncommon throughout the fracture, though. Moreover, the aperture shows larger variations towards the middle and on the right-hand side, as well as narrower structures throughout the rest of the fracture. Besides a slight bending towards the edges of the fracture, the model further shows a complex and heterogeneous geometry and aperture distribution, revealing major steps within the topography. Furthermore, plateau-like structures of major aperture (> 0.8 mm) are observed in the central part. There are also significant topographic differences and variations within the fracture geometry, partly correlating with the already observed bending. Indicated by a topographic "depression", correlating with a major step located right next to the third inlet. A chain of higher topography on the other hand is located diagonally from the central left towards the upper-central area. Interestingly though, these topographic features do not always correlate with higher or lower aperture values.

2.3. Flow experiments

The spatial distribution of multiple fluid inlets and outlets provides different combinations of input-output dipoles. In accordance to the synthetic equilibrium water used by (Stoll et al., 2019), the injection fluid was set up with pH 5.6, NaCl 3.04 10^{-4} mol/l, KCl 5.43 10^{-4} mol/l, and NaF 1.3 10^{-4} mol/l (i.e. total dissolved salt: 0.0638 g/L). This hydro-chemical composition however is different to the reservoir fluid circulating in the Soultz-sous-Forêts EGS (e.g. (Sanjuan et al., 2016)). A pulse of 1 mL was labeled with values between 62 and 89 MBq $^{18}F^{-}$and injected from the bottom into the fracture. Continuous flow rates of 12 mL/h were applied for three experiments (cases 2 to 4), similar to those conducted by (Stoll et al., 2019). In addition, one experiment was conducted at a reduced flow rate of 6 mL/h (case 1), in order to achieve a higher resolution of the propagating tracer front. The activity at the outlet was constantly monitored with a gamma flow-through counter (Elysia-Raytest©, GABI, radioactivity-HPLC-flow-monitor). Unfortunately, the maximum count rate of the gamma log is limited to 5 10^5 counts, which was exceeded at some point in the experiment. A summary of the experimental settings is given in Table 1.

2.4. Data processing

The μ-CT images were post-processed with the Avizo-Software, covering co-registration with PET, segmentation of the fracture, computation of the thickness map (aperture), and the central fracture topography. Additionally, the μ-CT image was downscaled to PET-resolution serving as geometry database for attenuation and scatter correction (Zakhnini et al., 2013). By downscaling the segmented μ-CT image to PET-resolution with box-filtering, we computed a porosity image corresponding to the coarser resolution of the PET.

It should be noted that the μ-CT-resolution of 72.6 μm is coarse with respect to the size of micro-fissures (< 72 μm) and hence these can remain undetected. Micro fissures were therefore excluded from the porosity determination, although these structures could possibly provide additional advective transport pathways.

The ClearPET images were calculated from the coincidence-LMFs with the help of the OEM software. This was considerably improved with respect to the requirements of dense media with functionality from the open-source STIR-library (Kulenkampff et al., 2016; Jacobson et al., 2000; Thielemans et al., 2012; Weber et al., 2006). Dependent on the total record length of an individual experiment, multiple LMFs with a frame length of 20 min each were recorded for every approach. In order to achieve a more suitable temporal resolution, those were then reframed to 1 min. The PET-data was then corrected with respect to random events, dead-time, sensitivity ("normalization"), decay, attenuation, and Compton scatter (Kulenkampff et al., 2016). Attenuation and scatter correction were conducted with the μ-CT-image, scaled to PET resolution (1.15 mm), and calibrated in mass-attenuation units at the energy of the annihilation photons (511 keV). Finally, the images were calibrated with respect to the injected activity.

Shortening of the frames causes fewer events per frame, and thus a higher background noise. This becomes more significant in later frames when the amplitude is amplified by decay correction. Therefore, the data eventually contains higher errors towards later times of the experiments.

The suite of PET-frames corresponds to a process tomogram of the fluid propagation. These tomograms could be directly compared to the fluid propagation from μ-CT-based model simulations. However, they also provide direct insights into flow variables, like local effective porosity, flow path geometry, and local flow rates or velocities (Kulenkampff et al., 2008; Kulenkampff et al., 2018). This data is derived by a

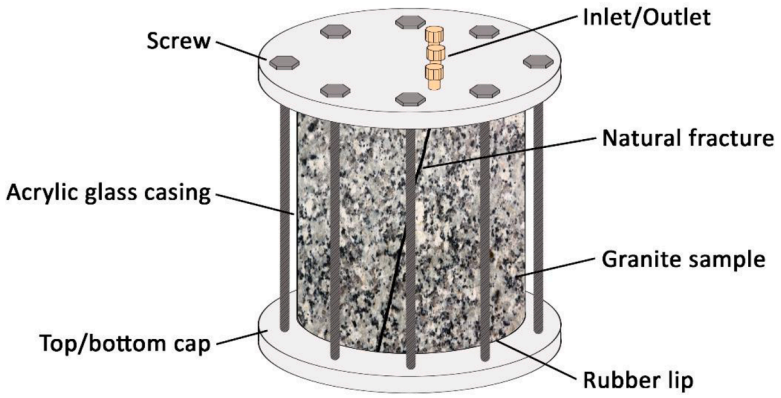

Fig. 1. Sketch of the drill core cell used during the experiments. Images of the core are provided in the supporting information (see SI-1 and SI-2).

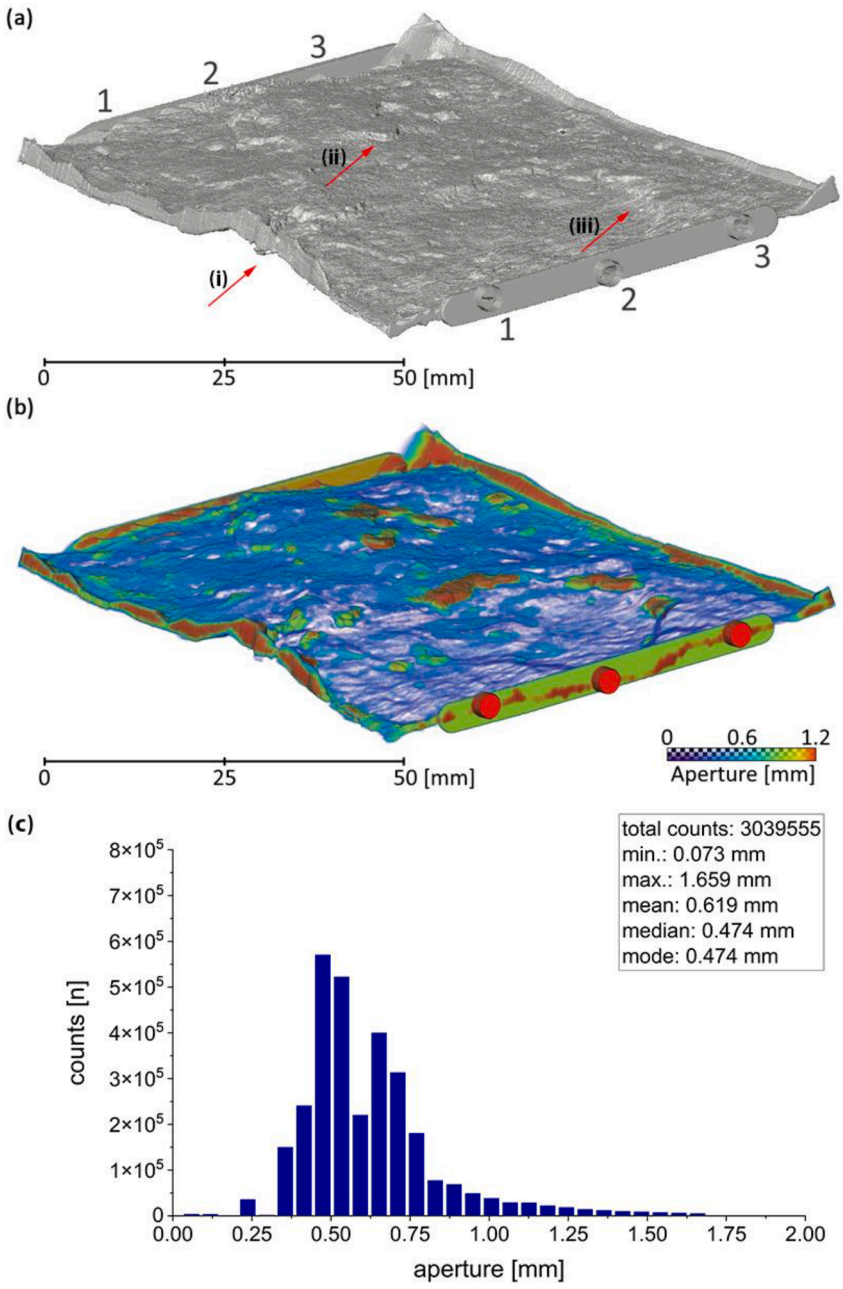

Fig. 2. Segmented fracture model with a resolution of 72.6 μm, shown as (a) a nearly continuous isosurface and computed from that, (b) a volume-projection of the aperture distribution. The numbers 1 to 3 represent the in- and outlets at the bottom and top of the sample used during the experiments. In (a) topographic highlights like bending at the left edge of the fracture (i), a topographic plateau within the central part of the fracture (ii), and a major topographic step just above the third inlet at the lower right-hand side (iii) are indicated by red arrows. (c) shows the aperture distribution as a histogram, excluding the in- and outlets, as well as the sealed border regions of the fracture.

Table 1
Summary of the experimental settings of the PET flow-through experiments.

Case	Flow rate (mL/h)	Dipole input	Dipole output	Injected activity (MBq)
1	6	1	1	61.7
2	12	1	1	71.208
3	12	1	3	74.083
4	12	3	3	88.823

special tracking algorithm based on the concept of optical flow, which acts on these 4D data sets and takes particular issues of the PET-data into consideration. Such issues are background noise and gaps in the propagation patterns that are due to an underrun of the detection threshold (e.g. 10 events/image point) where the tracer becomes widely distributed over a large volume or where the local velocity is very high. This GeoPET Flow software was developed by (Eichelbaum et al., 2015). Intended as a special type of segmentation procedure, the algorithm considers only the 4D-PET-data, without provisions for physical principles or models, like causality, dispersion, and mass conservation. The most significant variable reconstructed by this program is the local flow rate. Computation of local velocities requires the porosity per voxel. Local effective porosity can be principally estimated from the maximum activity per voxel, but these are erroneous and distorted by dispersion effects. This is why we apply the porosity that is derived from the μ-CT image in order to calculate the velocity direction and magnitude.

2.5. Numerical formulation: Governing equations, boundary, and initial conditions

The numerical 2.5D model of Stoll et al., 2019 (Stoll et al., 2019) is slightly modified to account for the decay reaction of $^{18}F^-$ and the boundary conditions of our experimental set-up experiment. Thus, the governing equations that determine the flow field are the continuity

equation and the momentum balance equation for an incompressible flow (i.e. Navier-Stokes):

$$\rho\nabla\cdot\boldsymbol{u} = 0 \tag{1}$$

$$\rho(\boldsymbol{u}\cdot\nabla)\boldsymbol{u} = \nabla\cdot\left[-p\boldsymbol{I} + \mu\left(\nabla\boldsymbol{u} + (\nabla\boldsymbol{u})^{T}\right)\right] + \boldsymbol{f}_{SCA} \tag{2}$$

where ρ [kg/m^3] is the fluid density, $\boldsymbol{u}$ [m/s] the fluid velocity vector, p [Pa] the fluid pressure, μ [kg/(ms)] the fluid dynamic viscosity, I the identity matrix, and $\boldsymbol{f}_{SCA}$ [kg/(m^{2}s^2)] is an added resistance force term to the momentum balance equation that takes into account the influence of the aperture, the so-called shallow channel approximation:

$$\boldsymbol{f}_{SCA} = -12\frac{\mu\boldsymbol{u}}{a^2} \tag{3}$$

The equations are formulated as stationary since boundary conditions do not change during the simulation and the experiment is assumed to start from an equilibrated flow field. At the dipole input, a normal inflow constant velocity boundary condition is applied 3.8 10^{-3} m/s (i.e. a flow rate of 6 mL/h) and 7.5 10^{-3} m/s (i.e. a flow rate of 12 mL/h). At the output dipole, a constant gage pressure boundary condition with a value of 0 Pa (i.e. an absolute pressure of 1 atm) and with a suppress backflow constraint is imposed.

The concentration profile through time and space is determined by the advection-convection-reaction equation (Williams, 1996):

$$\frac{\partial c}{\partial t} = \nabla\cdot\boldsymbol{D}\nabla\mathrm{c} - \boldsymbol{u}\cdot\nabla\mathrm{c} - \lambda\mathrm{c} \tag{4}$$

where c [mol/m^3] is the concentration in space and time, $\boldsymbol{D}$ [m^2/s] is the diffusion tensor and λ [s^{-1}] is the decay constant with a value of 0.0001 s^{-1} (i.e. half-life 109.771 min). The diffusion tensor is considered to be isotropic, hence $D_{xy} = D_{yx} = 0$ m^2/s and $D_{xx} = D_{yy} = 1.372\ 10^{-9}$ m^2/s (Ribeiro et al., 2010). At the input dipole ($\partial\Omega_{input\ dipole}$), a variable concentration is given:

$$c\left(\partial\Omega_{input\ \ dipole},\ t\right) = \begin{cases} \mathrm{c}_0 e^{-\lambda t} & 0 < t < t_{stop} \\ 0 & t_{stop} < t \end{cases} \tag{5}$$

c_0 [mol/m^3] is the corrected injected concentration (i.e. residence time corrected for the dead volume). c_0 is obtained by transforming the injected activity (Table 1) into mols through the use of the specific activity of ^{18}F- (i.e. 6.337 10^{10} GBq/mol), and considering the decay from the injection point until the dipole input of the model. The “dead” volume between the injection point and the dipole input was estimated to be approx. 0.5 mL. Therefore, a radioactive decay time of 300 s for the flow rate of 6 mL/h and 150 s for 12 mL/h on the injected concentration was considered. The parameter t_{stop} is related to the 1 mL injected pulse. Hence, t_{stop}= 10 min if the flow rate is 6 mL/h and t_{stop}= 5 min if the flow rate is 12 mL/h. The Dirichlet boundary condition, Eq. (5), is multiplied by a sigmoid function in order to decrease possible numerical oscillations, smoothing the sharp transition. At the output dipole, an outflow boundary condition is specified.

The initial conditions for the unknown variables ($\boldsymbol{u}$, p *and* c) are set to 0 in the whole domain.

3. Results

3.1. Visualization of temporal flow pattern

We investigate four cases (1–4) of fracture flow with varying dipole setups ((1–1), (1-3), (3–3)) and flow rates of either 12 mL/h or 6 mL/h, respectively. The mean velocity, Peclet number and Reynolds numbers obtained from the numerical simulations can be seen in Table 2. As an example, Fig. 3 shows the development of the tracer pattern of case 1 (1–1) inlet-outlet configuration with a flow rate of 6 mL/h. Compared to the other experiments with higher flow rate, this setup shows the propagating tracer with the highest amount of detail, because the temporal resolution is higher and the noise level lower than with the higher flow rates. Furthermore, the calculated layer-wise (z-direction) activity over time shows that the similarity between adjacent trans-axial slices is higher and provides a smoother database for the reconstruction of flow paths. Considering a delay of 300 seconds due to the dead volume before the inlet; in the first 100 s (i.e. 420 s) we observe the evolution of marked flow paths with high tracer concentration. In the later phase, propagating towards the outlet, the tracer pattern disperses over the whole width of the fracture, still showing distinct connected zones with high tracer concentration.

Table 2
Mean velocity, mean Peclet number, and mean Reynolds number for all numerically simulated cases. Diffusion: 1.372 10^{-9} m^2/s; characteristic length (i.e. mean aperture): 4.95 10^{-4} m; kinematic viscosity of water: 10^{-6} m^2/s.

Case	mean velocity [m/s]	mean Peclet number	mean Reynolds number
1	4.97 10^{-5}	17.93	2.46 10^{-2}
2	9.81 10^{-5}	35.39	4.86 10^{-2}
3	1.01 10^{-4}	36.58	5.03 10^{-2}
4	9.2 10^{-5}	33.26	4.56 10^{-2}

Highlighted by this example, the alignment of Fig. 3 indicates the propagation of the tracer during the experiment. In the beginning, the tracer front develops a fan-like flow pattern with a splitting flow path towards the central parts of the fracture. Proceeding, the labeled fluid develops a more distinct tracer front and channeling behavior, propagating towards the open fracture and ultimately towards the outlet in the upper left corner of the cell. Noticeably, some areas of minor or no activity develop within the open fracture, creating localized but persistent shadow zones that can be observed for all experiments conducted, no matter what setup or flow rate was applied (compare Fig. 5). Two main discrepancies can be observed between the experimental and numerical results: a) the numerical results show a more extended zone of the radiotracer plume, and b) the results of the GeoPET show "preferential" paths which are not well captured by the numerical model.

3.2. Calculated streamlines

Pattern recognition in these spatio-temporal concentration distributions is an intricate task. Instead, we derived the most likely flow path distribution with the GeoPET Flow software, computing the effective porosity for the particular process conditions, and the vector field of the flow rate; both with direction and magnitude.

Fig. 4 shows the calculated streamlines projected onto the fracture aperture model (color-coded) for all experiments conducted. As some preferential flow paths are leading directly from the individual inlets towards the outlets, other streamlines indicate wider spreading and diverging flow features throughout the fracture for the most part. While especially the experiments with the higher flow rates (12 mL/h) tend to have a wider and more fan-like flow pattern developing from their inlets towards the open fracture, the setup for case 1 shows a more distinct flow towards the outlet. The setup of case 4 shows a particular streamline pattern, initially evolving a small fan-like structure near the inlet, then showing a bimodal propagation over the whole breadth, and finally following the preferential flow paths of the other inlet-outlet configurations.

The streamlines also indicate obstacles like a bean-shaped shadow zone (see e.g. arrow Fig. 4, d), which are persistent in all experiments.

The streamlines develop a channeling behavior and flow most likely through the areas of least resistance, depending on multiple parameters like the aperture value, topographic tortuosity, or other geometry-related structures; obviously not controlled by a single parameter. A common feature like preferential flow behavior can be observed for areas like the direct path between the left in- and outlet (1), whereas other areas, e.g. the topographic step in the lower right corner (near inlet

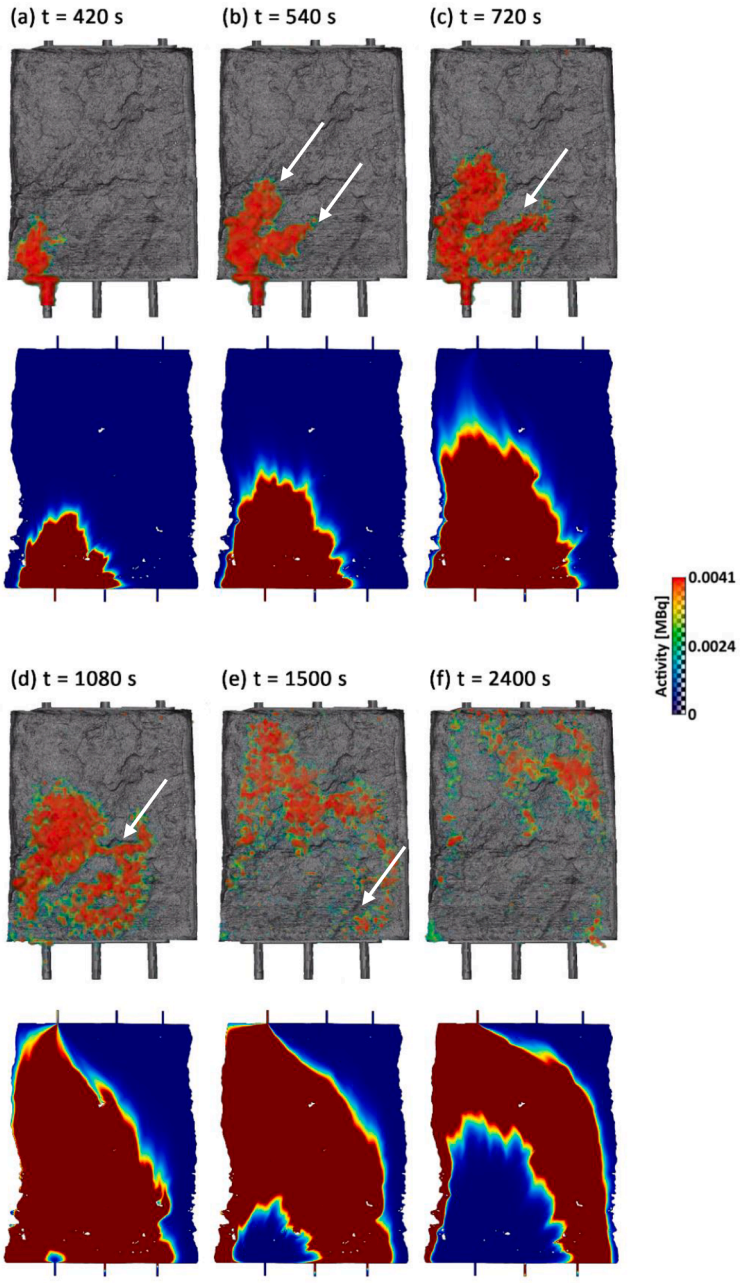

Fig. 3. Alignment of different stages during the GeoPET (isosurface projections) and the numerical analog experiment (COMSOL) with the connection setup of case 1. Starting at an early stage of the experiment, (a) shows the very beginning of the radiotracer being injected into the fracture at t = 420 [s]. (b) to (d) illustrate the splitting of the tracer front (channeling) within the sample, with (e) being the time when the tracer reaches outlet 1 in the upper left corner of the cell. The white arrows highlight some of the more important flow paths (e.g. channeling behavior or shadow zones) that can be observed for all experiments.

3), or the bean-shaped structures in the lower central and upper central-right are mostly flown around (shadow zones), even though they would correlate with wider aperture values.

3.3. Flow rate and aperture correlation

To investigate potential flow rate and aperture correlations, orthographic projections of the individual GeoPET flow rates were projected onto the aperture or porosity distribution, respectively. Revealing no major correlations, the calculated flow rates do not always match with a corresponding porosity, expecting higher flow rates for wider aperture values and vice versa, under the same boundary conditions.

For a quantitative correlation of the local flow rate and its aperture dependency, the flow rate value Q must be divided by the local porosity φ derived from μ-CT. Derived from the orthographic flow rate projections onto the aperture width, we were able to compute a correlation histogram of the flow rate, with respect to its aperture distribution. Illustrated in Fig. 5, no clear linear in- or decreasing correlation between the aperture width and a corresponding rise or decrease of the flow rate values can be observed. However, there is a distinct clustering trend of flow rate values for all experiments. Although with slight variations, the bulk of data ranges around 0.02 to 0.05 mm^2. Showing unconformities with the measured average aperture distribution of our CT-model, the correlation plot does show agreement with both the statistical values reported by (Stoll et al., 2019), as well as the median and mode values of our CT-model. Subsequently, this leads to the presumption of having a flow path evolution dependency, which is affected by more additional parameters (e.g. geometry, topography, etc.). Shown PET results (Fig. 5) are limited to the significant value range of the measurements, in order to be reliably reconstructed (e.g. a jump over many voxels from one frame to frame, i.e. high velocity).

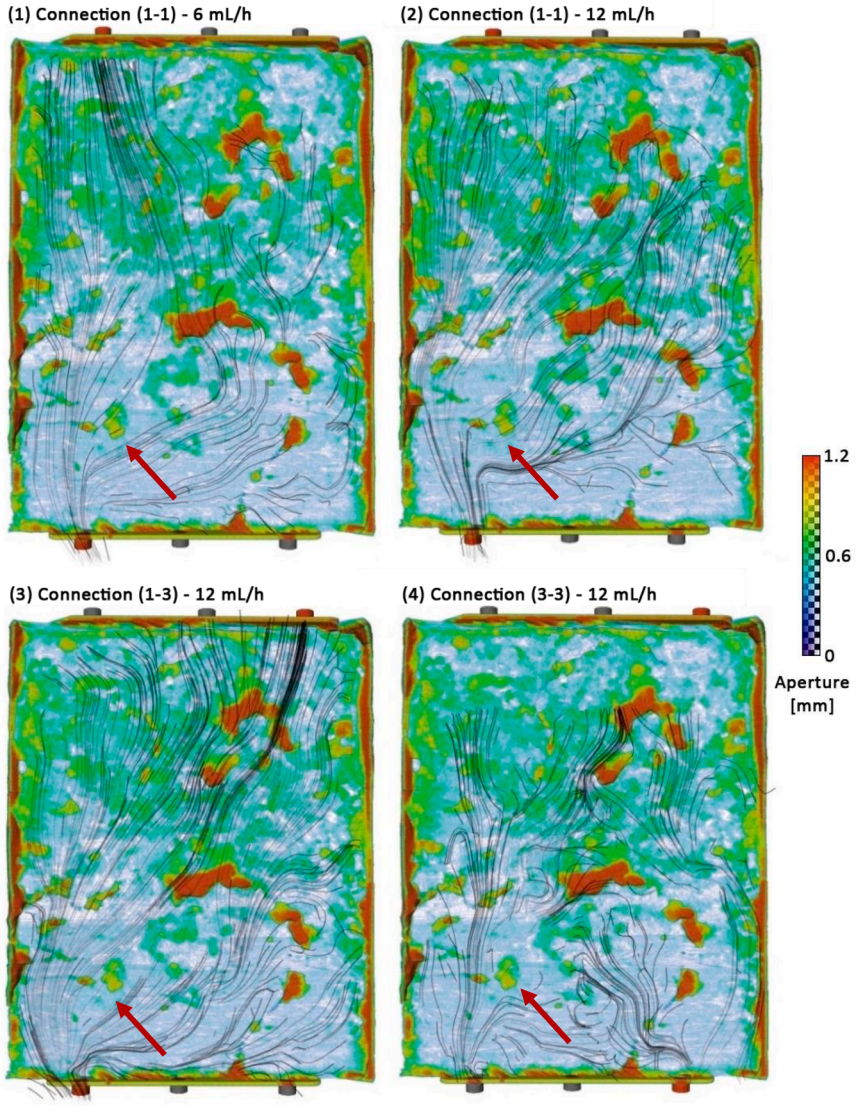

Fig. 4. Projected onto the aperture distribution of the fracture (comp. Fig. 2, b) and illustrated from the data of the dissected timesteps, the image shows the calculated most probable flow paths (black lines) for all experiments conducted. The data shows a mostly distinct channeled distribution from the in- towards the outlets for all experiments. Indicated by some preferential flow paths, the data highlights paths of lower resistance, following certain topographic and/or aperture-related features. Used inlets (bottom) and outlets (top) are highlighted in red. Note, however, that there was a computational issue with the calculation of the streamlines for case 4, which lead to a data loss in the upper part of the fracture. The red arrows mark a common area with minor flow for cases 1-4.

3.4. Breakthrough curves

Fig. 6 shows the comparison of the first arrival time of the breakthrough curves between the experiment and numerical results. The experimental first arrival time of the breakthrough curves was obtained from the gamma counter. The numerical first arrival time of breakthrough curves are calculated at the output dipole. The numerically calculated values are modified in order to account for the “dead” volume (i.e. 0.5 mL) between the output dipole and the gamma counter, similar to the corrected injected concentration (c_0).

The best agreement between experimental and numerical results is obtained in case 1 (flow rate 6 mL/h), while a time shift disagreement occurs for cases 2, 3, and 4 (flow rate 12 mL/h). The distance between cases 2, 3, and 4 for the numerical cases is larger than the one between the experimental cases (i.e. distance between dash-dotted lines and the distance between dots). This seems to indicate that the first arrival concentration of the model is more sensitive to the dipole configuration than the experimental case.

Since the activity was measured at the injection point and not at the dipole of the fracture. We do analyses the sensitivity of small changes in the corrected injected concentration (c_0) regarding the first-arrival time of the breakthrough curve. Fig. 7 shows that small changes on c_0 do not affect the first arrival of the breakthrough curve for cases 1 and 4, but in case 2 and specifically in case 3 it is possible to observe how variations of c_0 and therefore variations on the "dead" volume might have an impact on the model results. Case 4 has the highest discrepancy between the model and experimental results regarding the first arrival of the concentration. The numerical first arrival of case 4 is indeed faster (before 200 s) than the other cases (after 200 s). Since Case 3 has a larger path than the other cases, it will have in principle more heterogeneity, which could explain how the different c_0 affects the breakthrough curve.

4. Discussion

As our experiments reveal different flow path behaviors for different dipole and flow rate configurations, both the flow pattern and correlating flow rates show distinct dependencies on multiple parameters. While the development of flow channeling and similar preferential flow pattern can be observed for all experiments that were conducted, higher flow rates generally cause dispersion or diversification, respectively. Lower flow rates on the other hand result in a more localized flow pattern. Furthermore, an influence of the fracture aperture and the topographic features on the flow field can be perceived. Inactive areas (< 10 events/min), or shadow zones, could be observed for all experiments at similar locations. As the evolving flow paths can be determined to a preferential path of least resistance, preferential flow rates indicate

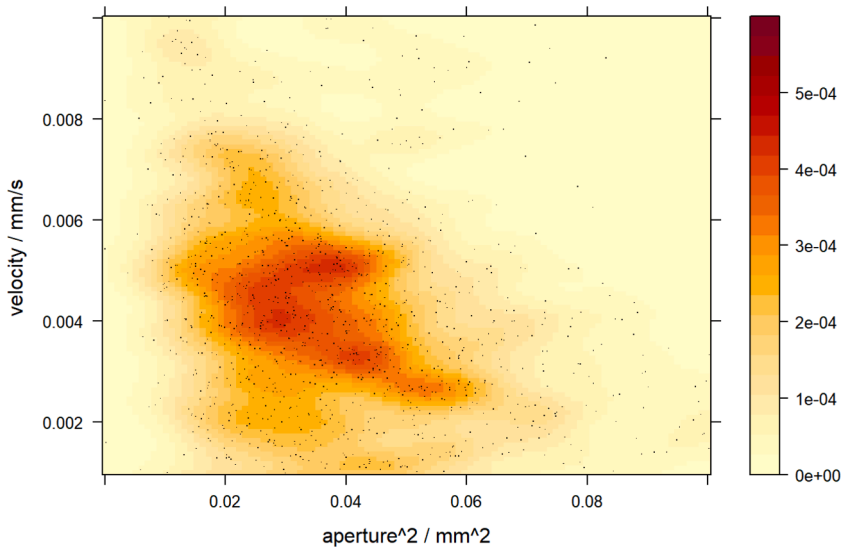

Fig. 5. Quantitative correlation histograms of the flow rate values derived from the Poiseuille law with respect to their spatial aperture distribution exemplified on the setup of case 1. Shown as point cloud denoting the velocity [mm/s] and the quadratic relation to the aperture width [mm^2]. The color-bar represents the normalized frequency density.

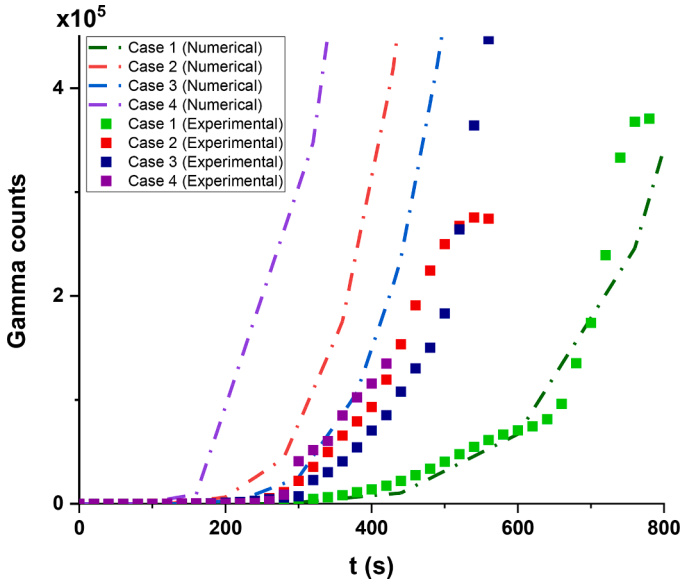

Fig. 6. Comparison between numerical and experimental breakthrough curves. Numerical results are given by dash-dotted lines, while experimental results are depicted by squared dots. Cases 1 to 4 are defined in Table 1.

some clustering for a certain aperture range. More comprehensive parameters like the surface roughness and PET isotope-mineral surface interactions might have a subordinated impact but were not part of the scope.

4.1. Influences on the flow pattern

While the aperture distribution and its consistency crucially affect the flow pattern for all experiments in a similar way, some areas are likely influenced by additional parameters. Furthermore, some features of the major flow paths appear to be invariable with respect to the input-output conditions, which are partly controlled by the aperture distribution, and partly by the surface topography (i.e. roughness and curvature).

A common feature are zones of minor activity (below detection limit) or no flow (shadow zones) at fixed locations for all experiments conducted. These shadow zones appear e.g. near the inlets 1 and 3, as well as towards the central and upper-central right area of the fracture (see Fig. 4). Again, the shadow zones appear to correlate with variations of the aperture and topographical features, like steep steps, correlating with "touching areas" described by (Stoll et al., 2019).

Assuming a low-stress laminar flow (Reynolds number: $\sim 10^{-2}$, see Table 2), due to the generally low flow rates applied, the flow pattern is likely controlled by the aperture distribution, then by geometrical effects (Cook, 1992). Our experimental observations of the flow evolution however do not confirm this simple assumption, but rather indicate a stronger influence of additional parameters, like the surface topography and dispersion in porous media (Yang et al., 2021).

Moreover, the transport of solutes in fractured rocks is affected by advective-dispersive transport, which is dominant in the fracture, as well as diffusive transport, which is dominant in the unfractured matrix. In the case of our numerical simulations, the mean Peclet number is around 35 ± 2 in cases 2 to 4 and 18 in case 1 (see Table 2). Since the matrix diffusion length of our fracture is short (x ≈ 1.2 mm; below the resolution of the GeoPET), matrix diffusion was not investigated. However, it plays a role as it has retention effects in crystalline rocks (Grisak and Pickens, 1980; Eichinger et al., 2020). It nevertheless may be relevant, as a diffusive transport can be expected at higher concentrations in close surface proximity for crystalline rock, though (Ohlsson, 2000).

4.2. Fracture surface impacts

The effective surface that is exposed to flow (flow-wetted surface) is a main controlling factor for the matrix diffusion and sorption of dissolved elements in the transport fluid within fractures (Larsson et al., 2012). Highly sensitive to the smallest variations, the flow pattern can be influenced anywhere in the cross-section. Due to its high sensitivity though, the PET-method allows an investigation of migration-relevant flow path evolution (flow-wetted surfaces).

As Fig. 5 indicates, no direct correlation was observed between the aperture and flow velocities plotted. This however might for once be given by measurement uncertainties, but also the application of the μ-CT provides the so-called mechanical aperture (Chen et al., 2000) instead of the hydraulic aperture. This on the other hand indicates the defective application of the cubic law approach for rough fracture surfaces, with

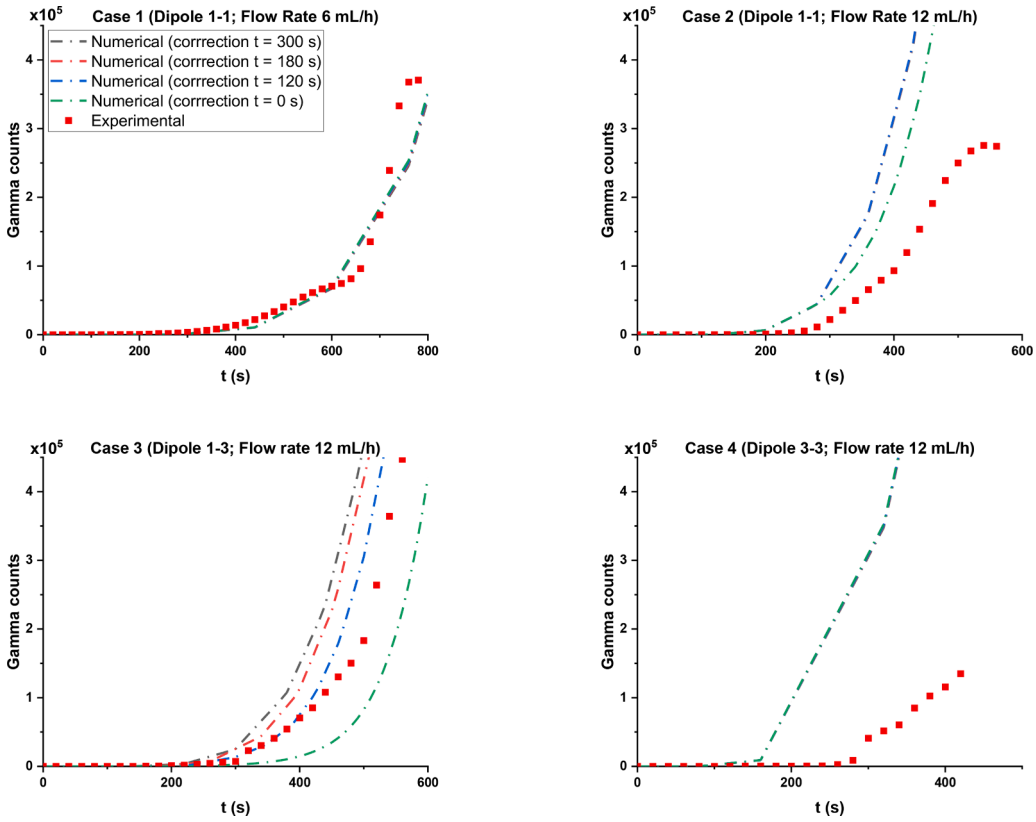

Fig. 7. Breakthrough curves for cases 1–4 assuming different decay times between injected concentration and dipole input, and therefore different corrected injected concentrations (c_0). A t= 0 s indicates that no decay correction has been used, namely, the injected concentration is c_0. A t= 300 s correspond to the corrected injection of Figs. 5 and 6 were the "dead" volume before the injection is 0.5 mL for a 6 mL/h flow rate.

such discrepancies already described by e.g. (Zimmerman and Bodvarsson, 1996). Moreover, (Hakami and Larsson, 1996) state deviation ratios between calculated and measured flow, further illuminate the observed discrepancies for our 3D data set.

Another factor to consider is the mineral surface roughness of the fracture. Surface roughness can be described as fluctuation around a specific surface solid, larger than the interatomic distance (Rahimi et al., 2012). While the mineral habitus, grain size, and cleavage can highly attribute to the individual surface roughness of a mineral, the different surface roughness may influence the flow path evolution within the flow cell. In the case of the granite sample from Soultz-sous-Forêts, potential alteration processes can be caused by natural fluid interactions (Pauwels et al., 1993), as well as hydrothermal alteration, dissolving significant amounts of biotite, plagioclases, and Alkali-feldspars (Eggeling et al., 2013). Formed by secondary phase formation on fracture surfaces, a hydrothermal alteration can be observed due to natural fluid circulation within the EGS reservoir, resulting in the deposition of altered minerals such as illite, calcite, or secondary (Genter et al., 2003; Genter and Cuenot, 2009). Depending on the grain size and alteration, smaller and non-altered feldspars are described to have a generally smoother surface than larger and altered ones (Anbeek, 1992). Similar for quartz, the surface roughness decreases with a decrease in grain size, while the surface area successively increases (Rahimi et al., 2012; Anbeek, 1992). Due to the high alteration potential of mica, it might lose its solidity and subsequently its smooth surface, which can in turn result in a much more restraining impact on the flow path evolution. Furthermore, mica is likely to alter under the hydrothermal conditions of an EGS and the generation of pyrite (FeS_2) as a typical alteration product of mica is supported. As sulfur is naturally hydrophobic due to its low critical surface tension (~ 26–33 dyn/cm), it acts less retaining, though (Ozcan, 1992).

Another factor to consider is the heterogeneity of crystalline rock as is e.g. shown by a one-dimensional analytical solution for the mean value of temporal moments of residence time probability (Xu et al., 2001). As the impact of solute transport of heterogeneous mass transfer with the crystalline rock matrix alongside the flow paths is being discussed, it is said to have a significantly more pronounced effect than the macro-dispersion caused by the differentiation of flow paths. As our specimen is a fractured porphyritic granite with potential micro fissures, an impact of matrix diffusion should be considered. However, as the sample is described to have minor alteration and no pore-clogging minerals (e.g. clays) are expected within the fracture after an initial cleaning (Stoll et al., 2019), the fluid flow is most likely dominated by an advective-dispersive transport through the main fracture. This also matches with our GeoPET observations, as no direct evidence for micro fissure-related flow or matrix diffusion was observed.

Eventually, the dissection of data in one-minute-long frames is too short. Ideally, one frame per voxel of progress (= 1 mm per frame) must be applied. However, as the dissected frames show a progression of 5 mm per frame, we were not able to achieve this. Subsequently, the results show a statistical projection of the measured data, which is still reliable though.

Concerning THMC processes which couple physico-chemical interactions in reservoirs, thermal and chemical parameters are susceptible to change in the numerical model. However, PET only allows for limited thermal changes due to technical reasons, while mechanical changes are scale-dependent.

4.3. *Experimental and numerical discrepancies*

The disagreement between the experimental and numerical results (Figs. 6and 7) might be given by several sources of uncertainty such as the instrumentation accuracy, and sensitivity of the measured activity before injection and at the measured gamma counter. In addition, the

μ-CT segmentation of the fracture might provide different results based on the applied segmentation algorithm and user judgment (Reinhardt et al., 2022), turning out in different aperture values. Moreover, the numerical model does not account for the surface roughness which adds a source of dispersion (Bodin et al., 2003), and the surface curvature. The aperture values used on the added resistance force term (i.e. Eq. (3)) were provided by the μ-CT segmentation. The use of a hydraulic aperture can be more convenient and may take into account surface roughness (Barton et al., 1985). The numerical model might also be sensitive to small changes in corrected injected concentration (c_0) regarding the first arrival time of the breakthrough curve especially case 3. Besides, the injection function of the experiment and the one used in the numerical simulation (i.e. Eq. (5)) might differ.

The observed larger plume of the model in comparison to the experimental results (Fig. 3) might be explained by an overestimation of the concentration of the model. Stoll, Huber (Stoll et al., 2019) did already find disagreements between the experimental and modeled breakthrough curves for the unaltered fracture where the modeled breakthrough curves had a higher amount of concentration and longer residence time. Although we only have the first arrival time of the breakthrough curves for the experimental case, since the gamma flow counter is limited to 5 10^5 counts, we can extrapolate from Fig. 3 that a larger plume in the model implies a higher concentration on the breakthrough curve and longer residence time. The preferential paths observed in Figs. 3 and 4 cannot be captured with the current model. Modifications of the aperture field, such as forcing zones with zero aperture, could help to capture such behaviors.

5. Summary and conclusions

Our experimental flow field analysis in fractured granite, using the GeoPET technique, enabled the visualization of the flow paths and hydrodynamic behavior within a fracture in granitic rock of a geothermal reservoir. We were thus able to demonstrate the advantages and opportunities of GeoPET for observing in-situ flow processes under laboratory conditions.

The relationship between the aperture distribution and the flow path evolution was investigated. We conclude that the flow paths and their characteristics are qualitatively and quantitatively controlled by (i) fracture geometry, (ii) surface roughness, and (iii) topographic tortuosity.

The results show that the flow paths depend mainly on the fracture geometry and the applied flow rates, in addition to the localization of inflows and outflows. Generally, the flow pattern and the correlated flow rate distribution show varying degrees of dependence on several parameters, as conceptually illustrated in Fig. 8. The correlation of aperture size and flow shows no clear global increasing or decreasing dependence but rather a local dependence on aperture size. Therefore, we conclude a quantitatively important influence of the topographic curvature of the fracture. As curvature increases, the flow velocity distribution decreases. Therefore, the developing flow paths are most likely driven by preferring the path of least resistance and thus subsequently flowing around unfavorable aperture and local wall geometries, including surface steps, narrow bends, rough surfaces, etc.

Transferring the experimental flow data concerns a major challenge with respect to upscaled conditions of an EGS. When comparing tracer test flow velocities performed at Soults-sous-Forêts of e.g. (Sanjuan et al., 2006), natural flow conditions reveal turbulent flow velocities four orders of magnitude higher (m/s) than the laboratory GeoPET experiments laminar flow (mm/h) (comp. Table 2). While micro-scale preferential flow was observed for our PET experiments, increasing permeability is expected when upscaling to macro-scale of a natural fracture system, as paths of lesser resistance become more abundant.

Furthermore, our results show that some specific flow features, such as shadow zones or preferential flow paths, develop in a similarly stable manner in certain regions for all experiments, but they are not related to the applied process conditions, as they are not influenced by different inlet and outlet arrangements nor by the flow rates applied.

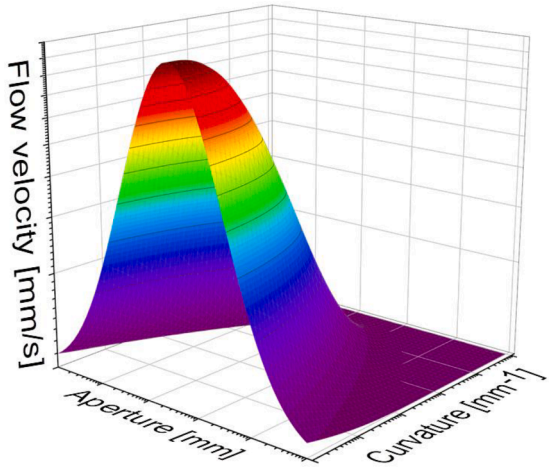

Fig. 8. Conceptual figure, illustrating the multi-parameter dependency of the velocity, with respect to the relative aperture distribution and the topographic curvature. Note, that the created planes of the three variables are only a hypothetic representation.

Discrepancies between the experimental and numerical models might arise due to different sources such as instrumental uncertainties or the limitations of the 2.5D model in including 3D parameters, e.g. topographic curvature, and roughness. The numerical model is able to capture the behavior of the tracer propagation. In certain cases, a good agreement between experimental and numerical is achieved, but unfortunately not always. Future studies dealing with the fluid flow and transport of radiotracers could be improved or refined by the implementation of the 3D topography in order to consider the fracture geometry as a whole, rather than just a simplification of the aperture width.

CRediT authorship contribution statement

Janis Leon Pingel: Data curation, Writing – original draft, Writing – review & editing, Investigation. **Johannes Kulenkampff:** Data curation, Writing – review & editing, Investigation. **Daniel Jara-Heredia:** Data curation, Writing – review & editing, Investigation. **Madeleine Stoll:** Data curation. **Wenyu Zhou:** Data curation. **Cornelius Fischer:** Supervision, Writing – review & editing, Funding acquisition. **Thorsten Schäfer:** Supervision, Writing – review & editing, Funding acquisition.

Declaration of Competing Interest

On behalf of all contributing authors, we hereby declare that no conflicts of competing interests are involved in this study.

Data availability

Data will be made available on request.

Acknowledgements

Janis Leon Pingel and Thorsten Schäfer gratefully acknowledge financial support from the German Federal Ministry of Economic Affairs and Climate Action (BMWK) under Contract 02E11759A (KOLLORADO-e^3). JK and CF gratefully acknowledge financial support from the European Union's Horizon 2020 research and innovation program under grant agreement No. 847593 (EURAD, WP FUTURE). Furthermore, we would also like to thank the reviewers for their helpful comments.

Supplementary materials

Supplementary material associated with this article can be found, in the online version, at doi:10.1016/j.geothermics.2023.102705.

References

Kulenkampff, J., et al., 2016. Geoscientific process monitoring with positron emission tomography (GeoPET). Solid Earth 7 (4), 1217–1231.

Baumann, T., Petsch, R., Niessner, R., 2000. Direct 3-D measurement of the flow velocity in porous media using magnetic resonance tomography. Environ. Sci. Technol. 31 (19), 4242–4248.

Ter-Pogossian, M.M., et al., 1975. A positron-emission transaxial tomograph for nuclear imaging (PETT). Radiology 114, 89–98.

Alauddin, M.M., 2011. Positron emission tomography (PET) imaging with 18F-based radiotracers. Am. J. Nucl. Med. Mol. Imaging 2, 55–76. **2012**.

van den Bergen, E.A., et al., 1989. Industrial applications of positron emission computed tomography. Nucl. Geophys. 3.

Benton, D.M., Parker, D.J., 1996. Non-medical Applications of Positron Emission tomography. Non-Invasive Monitoring of Multiphase Flows. Elsevier Science B. V.

Kulenkampff, J., et al., Application of high-resolution positron-emission-tomography for quantitative spatiotemporal process monitoring in dense material, in 7th World Congress on Industrial Process Tomography (WCIPT7). 2013: Krakow, Poland.

Kulenkampff, J., et al., 2008. Evaluation of positron-emission-tomography for visualisation of migration processes in geomaterials. Phys. Chem. Earth 33 (14–16), 937–942. Parts A/B/C.

Fernø, M.A., et al., 2015. Combined positron emission tomography and computed tomography to visualize and quantify fluid flow in sedimentary rocks. Water Resour. Res. 51 (9), 7811–7819.

Zahasky, C., et al., 2019. Positron emission tomography in water resources and subsurface energy resources engineering research. Adv. Water Resour. 127.

Stoll, M., et al., 2019. Experimental and numerical investigations on the effect of fracture geometry and fracture aperture distribution on flow and solute transport in natural fractures. J. Contam. Hydrol. 221, 82–97.

Huber, F., et al., 2012. Natural micro-scale heterogeneity induced solute and nanoparticle retardation in fractured crystalline rock. J. Contam. Hydrol. 133, 40–52.

Kohl, T., et al., 1997. Observation and simulation of non-Darcian flow transients in fractured rock. Water Resour. Res. 33 (3), 407–418.

Schill, E., et al., 2017. Hydraulic performance history at the Soultz EGS reservoirs from stimulation and long-term circulation tests. Geothermics 70, 110–124.

Kolditz, O., 2001. Non-linear flow in fractured rock. Int. J. Numer. Methods Heat Fluid 11, 547–575.

Geckeis, H., et al., 2004. Results of the colloid and radionuclide retention experiment (CRR) at the Grimsel Test Site (GTS), Switzerland – impact of reaction kinetics and speciation on radionuclide migration. Radiochim. Acta 92 (9–11), 765–774.

Brush, D.J., Thomson, N.R., 2003. Fluid flow in synthetic rough-walled fractures: Navier-Stokes, Stokes, and local cubic law simulations. Water Resour. Res. 39 (4).

Huang, N., et al., 2021. Development and application of three-dimensional discrete fracture network modeling approach for fluid flow in fractured rock masses. J. Nat. Gas Sci. Eng. 91, 103957.

Huyakorn, P.S., Lester, B.H., Faust, C.R., 1983. Finite element techniques for modeling groundwater flow in fractured aquifers. Water Resour. Res. 19 (4), 1019–1035.

Eker, E., Akin, S., 2006. Lattice Boltzmann simulation of fluid flow in synthetic fractures. Transp. Porous Media 65 (3), 363–384.

Tartakovsky, A.M., Meakin, P., 2005. A smoothed particle hydrodynamics model for miscible flow in three-dimensional fractures and the two-dimensional Rayleigh–Taylor instability. J. Comput. Phys. 207 (2), 610–624.

Li, T., Shiozawa, S., McClure, M.W., 2016. Thermal breakthrough calculations to optimize design of a multiple-stage Enhanced Geothermal System. Geothermics 64, 455–465.

Ziemons, K., et al., The ClearPET. Neuro scanner: a dedicated LSO/LuYAP phoswich small animal PET scanner, in IEEE Symposium Conference Record Nuclear Science 2004. 2004. p. 2430–2433.

Levin, C.S., Hoffman, E.J., 1999. Calculation of positron range and its effect on the fundamental limit of positron emission tomography system spatial resolution. Phys. Med. Biol. 44, 781–799.

Berger, M.J., et al., 2010. XCOM: photon Cross Section Database. NIST Standard Ref. Database 8. XGAM.

Sanjuan, B., et al., 2016. Major geochemical characteristics of geothermal brines from the Upper Rhine Graben granitic basement with constraints on temperature and circulation. Chem. Geol. 428, 27–47.

Zakhnini, A., et al., 2013. Monte Carlo simulations of GeoPET experiments: 3D images of tracer distributions (18F, 124I and 58Co) in Opalinus clay, anhydrite and quartz. Comput. Geosci. 57, 183–196.

Jacobson, M., et al., 2000. Enhanced 3D PET OSEM reconstruction using inter-update Metz filtering. Phys. Med. Biol. 45, 2417–2439.

Thielemans, K., et al., 2012. STIR: software for tomographic image reconstruction release 2. Phys. Med. Biol. 57 (4), 867–883.

Weber, S., et al., 2006. Image reconstruction for the ClearPET™ Neuro. Nucl. Instrum. Methods. Phys. Res. A 569 (2), 381–385.

Kulenkampff, J., et al., 2018. Time-lapse 3D imaging by positron emission tomography of Cu mobilized in a soil column by the herbicide MCPA. Sci. Rep. 8 (1), 7091.

Eichelbaum, S., et al., Quantifying 3D tracer velocity and porosity on core scale form 3D GeoPET image sequences, in IAMG 2015, 17th annual conference of the International Association for Mathematical Geosciences. 2015: Freiberg, Germany.

Williams, M.M.R., 1996. Radionuclide transport in fractured rock. Prog. Nucl. Energy 30 (3), 243–253.

Ribeiro, A.C., et al., 2010. Diffusion coefficients of sodium fluoride in aqueous solutions at 298.15 k and 310.15 k. Acta Chim. Slov. 57 (2), 410–414.

Cook, N.G.W., 1992. Natural joints in rock: mechanical, hydraulic and seismic behaviour and properties under normal stress. Int. J. Rock Mech. Min. Sci. 29, 198–223.

Yang, Y., et al., 2021. Effects of velocity and permeability on tracer dispersion in porous media. Appl. Sci. 11 (10), 4411.

Grisak, G.E., Pickens, J.F., 1980. Solute transport through fractured media 1. The effect of matrix diffusion. Water Resour. Res. 16 (4), 719–730.

Eichinger, F., et al., 2020. Profiles of chloride in matrix porewater as natural tracer for matrix diffusion in crystalline rocks. Appl. Geochem. 118.

Ohlsson, Y., 2000. Studies of Ionic Diffusion in Crystalline Rock, in Department of Chemical Engineering and Technology. Royal Institute of Technology, Stockholm, Sweden, p. 69.

Larsson, M., Niemi, A., Tsang, C.-F., 2012. A study of flow-wetted surface area in a single fracture as a function of its hydraulic conductivity distribution. Water Resour. Res. 48 (1).

Chen, Z., et al., 2000. An experimental investigation of hydraulic behaviour of fractures and joints in granitic rock. Int. J. Rock Mech. Min. Sci. 37 (7), 1061–1071.

Zimmerman, R.W., Bodvarsson, G.S., 1996. Hydraulic conductivity of rock fractures. Transp. Porous Media 23, 1–30.

Hakami, E., Larsson, E., 1996. Aperture measurements and flow experiments on a single natural fracture. Int. J. Rock Mech. Mining Sci. Geomech. Abstract 33 (4), 395–404.

Rahimi, M., et al., 2012. Influence of the roughness and shape of quartz particles on their flotation kinetics. Int. J. Miner. Metall. Mater. 19 (4), 284–289.

Pauwels, H., Fouillac, C., Fouillac, A.-.M., 1993. Chemistry and isotopes of deep geothermal saline fluids in the Upper Rhine Graben: origin of compounds and water-rock interactions. Geochim. Cosmochim. Acta 57, 2737–2749.

Eggeling, L., et al., 2013. Impact of natural radionuclides on geothermal exploitation in the Upper Rhine Graben. Geothermics 47, 80–88.

Genter, A., et al., 2003. Typology of potential Hot Fractured Rock resources in Europe. Geothermics 32 (4–6), 701–710.

Genter, A., Cuenot, N., 2009. Overview of the Current Activities of the European EGS Soultz Project. ES-Geothermie.

Anbeek, C., 1992. Surface roughness of minerals and implications for dissolution studies. Geochim. Cosmochim. Acta 56, 1461–1469.

Ozcan, O., 1992. Classification of minerals according to their critical surface tension of wetting values. Int. J. Miner. Process. 34, 191–204.

Xu, S., Wörman, A., Dverstorp, B., 2001. Heterogeneous matrix diffusion in crystalline rock - implications for geosphere retardation of migrating radionuclides. J. Contam. Hydrol. 47, 365–378.

Reinhardt, M., et al., 2022. Benchmarking conventional and machine learning segmentation techniques for digital rock physics analysis of fractured rocks. Environ. Earth Sci. 81 (3), 71.

Bodin, J., Delay, F., de Marsily, G., 2003. Solute transport in a single fracture with negligible matrix permeability: 1. fundamental mechanisms. Hydrogeol. J. 11 (4), 418–433.

Barton, N., Bandis, S., Bakhtar, K., 1985. Strength, deformation and conductivity coupling of rock joints. Int. Rock Mech. Mining Sci. Geomech. Abstracts 22 (3), 121–140.

Sanjuan, B., et al., 2006. Tracer testing of the geothermal heat exchanger at Soultz-sous-Forêts (France) between 2000 and 2005. Geothermics 35 (5–6), 622–653.